Periodic structures for melting enhancement
observation of critical cell size and localized melting

Zhao, Chunrong; Opolot, Michael; Liu, Ming; Wang, Ji; Bruno, Frank; Mancin, Simone; Hooman, Kamel

DOI
10.1016/j.ijheatmasstransfer.2022.123107

Publication date
2022

Document Version
Final published version

Published in
International Journal of Heat and Mass Transfer

International Journal of Heat and Mass Transfer 195 (2022) 123107

Contents lists available at ScienceDirect

International Journal of Heat and Mass Transfer

journal homepage: www.elsevier.com/locate/hmt

Periodic structures for melting enhancement: observation of critical cell size and localized melting

Chunrong Zhao[a,*], Michael Opolot[a], Ming Liu[b], Ji Wang[b], Frank Bruno[b], Simone Mancin[c], Kamel Hooman[d]

[a] School of Mechanical and Mining Engineering, The University of Queensland, Brisbane, QLD 4072, Australia
[b] Future Industries Institute, University of South Australia, Mawson Lakes Boulevard, Mawson Lakes, SA 5095, Australia
[c] Department of Management and Engineering, University of Padova, Stradella S. Nicola, 3, Vicenza 36100, Italy
[d] Department of Process and Energy, Delft University of Technology, Leeghwaterstraat 39 2628 CB Delft, The Netherlands

ARTICLE INFO

Article history:
Received 5 November 2021
Revised 14 March 2022
Accepted 2 June 2022

Keywords:
PCM melting
Periodic structure
Critical cell size

ABSTRACT

The use of metallic periodic structures was considered for melting rate enhancement of a phase change material (PCM) contained in a rectangular enclosure isothermally heated from the side. The critical (optimized) cell size, or pore size, of a periodic structure with fixed porosity, realising the shortest melting time by maximizing the convection and conduction heat transfer rate into the PCM, was studied. Furthermore, the effects of material properties (copper, aluminium, nickel, and stainless steel), enclosure length, wall-melting temperature difference and porosity were numerically investigated. It was observed that increasing porosity and/or reducing thermal conductivity enlarged the critical cell size (i.e. the optimal cell size that minimizes the melting time). The critical PPIs (pores per inch) of copper and aluminium periodic structures for all studied porosities were 10; for nickel, the critical values were 10 PPIs for porosity values of 0.75, 0.8 and 0.85 while it reduces to 5 PPI for the highest porosity considered here being 0.95. Interestingly, showing a different trend, the critical PPI of stainless-steel structures was 5 for the lowest porosity (0.75) and reduced to 3 for higher porosities. The results clearly demonstrated localised melting which was observed in all periodic structures except for the 10 PPI stainless-steel case. Scattered melting islands are observed as opposed to a moving interface when $\phi=(d_p/L)\sqrt{\alpha_{\text{ligament}}/\alpha_{\text{PCM}}} > 1$. For such cases, localized melting occurs and the PCM is melted at the ligaments away from the heated wall before the melt front reaches those ligaments.

1. Introduction

Latent heat thermal energy storage (LHTES) systems, utilizing solid-liquid phase change materials (PCMs), have many industrial applications, such as concentrated solar power (CSP) [1], electronic devices [2], thermal management of buildings [3] and electric vehicles [4]. Taking advantages of its high latent heat of fusion and low temperature variation during operation makes LHTES systems very popular. However, the poor thermal conductivity of most PCMs deteriorates the heat exchange rate [5]. Heat transfer enhancement techniques for PCM systems are therefore required to accelerate the charge and discharge process of LHTES systems [6–8], which can be classified into three categories, that is, enhancing PCM conductivity, extending heat transfer surface area and improving process uniformity [9]. The second type consists mainly of brazing highly conductive fins, porous matrices and additively manufactured periodic structures to the heated surfaces, e.g. the pipe wall containing the heat transfer fluid (HTF). These practices stretch numerous fast heat transfer paths into the PCM while the segmented PCM size is crucial since it closely relates to the enlarged heat exchange area by these pathways.

For finned-PCM systems, the fin number (or spacing) can be equivalent to the size of compartmentalized PCM if the fin length and volume percentage are fixed. They were extensively investigated and optimized for different-shaped PCM containers, for instance, rectangular or tubular enclosures. For a rectangular tank heated from the top side, Levin et al. [10] numerically optimized a PCM-based heat sink with internal fins to cool down electronic devices. Fixing the fin length, the optimized fin number densities were obtained for different fin volume fractions. Once the fin num-

Abbreviations: CFD, computational fluid dynamics; CSP, concentrated solar power; HTF, heat transfer fluid; PCM, phase change material; PPI, pores per inch; PRESTO!, pressure staggering option; QUICK, quadratic upstream interpolation for convective kinematics; SIMPLE, semi-implicit method for pressure linked equation; SS, stainless steel; LHTES, latent heat thermal energy storage.

* Corresponding author.
E-mail addresses: chunrong.zhao@uq.edu.au (C. Zhao), K.hooman@TUDelft.nl (K. Hooman).

https://doi.org/10.1016/j.ijheatmasstransfer.2022.123107
0017-9310/

Nomenclature

A	mushy zone constant, kg/(m^3·s)
c_p	specific heat, J/(kg·K)
d_f	ligament diameter, m
d_p	pore (cell) diameter, m
g	gravitational acceleration, m/s^2
h	specific enthalpy, J/kg
h_{sf}	latent heat of fusion, J/kg
H	enclosure height, m
k	thermal conductivity, W/(m·K)
L	enclosure length, m
P	Pressure, Pa
Ra	Rayleigh number, defined as $g\beta(T_w - T_m)H^3/\alpha\nu$
t	time, s
T	temperature, K
u, v, w	superficial velocities in $\boldsymbol{x}$, $\boldsymbol{y}$ and $\boldsymbol{z}$ directions, m/s

Greek letters

α	thermal diffusivity, m^2/s
β	thermal expansion coefficient, 1/K
γ	liquid phase fraction
ε	porosity
μ	dynamic viscosity, Pa·s
ρ	density, kg/m^3
σ	computational constant

Subscripts

eff	effective
l	liquidus
ref	reference
s	solidus
w	wall

ber density increased beyond 0.2 fins/mm, it was found that the number of fins per unit system width was insignificant while the fin length and volume percentage were significantly affecting the critical time, which was the time required for the interface temperature to reach the maximum allowable temperature. For a basally heated rectangular enclosure, Kalbasi et al. [11] studied the optimum vertical fins number in PCM-based heat sinks. Different parameters including the enclosure height, fin thickness and input heat fluxes were investigated to determine the optimal number of fins, which was eventually corelated as $N_{opt} = [L/(d_f + d_{p,opt}) - 1]$. Note that L denoted the length of PCM enclosure and the optimal fin spacing ($d_{p,opt}$) was a function of the enclosure height, fin thickness (d_f) and heat flux. It concluded that the optimal fin number density could decrease if increasing fin thickness and enclosure height and/or reducing heat fluxes. For a rectangular PCM with lateral heating, Sharifi et al. [12] numerically studied the effect of fin spacing and fin length (L_f) on the melting rate enhancement and thus raised two distinct stages, rapid (conduction-dominant) and slow (convection-dominant) melting regimes, for the entire duration of melting. It turned out that the transition point was when the melt front reached the fin length, therefore, a longer$L_f$led to a higher percentage of rapid regime, thus a faster averaged melting rate. As for a vertically-oriented tubular PCM, Yang et al. [13] numerically investigated melting enhancement using annular fins under fixed fin volume ratio (2%) and fin length (L_f = 10 mm), where an increased fin number was associated to smaller fin thickness and compartmentalized PCM size. The simulated results indicated that the melting time was firstly diminished from approximately 6200 s to 3200 s when the fin number augmented from 3 to 31. Subsequently, increasing the fin number from 31 to 43 led to an increasingly elongated melting time to around 4000 s and the value of melting time kept unvarying afterwards for the fin number enlarged from 43 to 67. On the other hand, for a horizontal tubular container, Zhao et al. [14] numerically investigated effects of fin number density on melting rate enhancement under constant fin-to-PCM volume ratio within a horizontally oriented annular enclosure. The simulated results suggested that the melting time exhibited a parabolic trend as fin number density increased and the optimal fin number density was 16, which shortened the melting time by over 60%, compared to the pure PCM case. Moreover, other fine-tuning strategies (for example, elongating fin length and narrowing down fin spacing at the lower part) only provided limited further melting rate enhancements while the tree-like branching fins inversely elongated the melting time. To summarize, for fin technology, increasing fin number (or reducing fin spacing) could result in a faster melting rate until reaching an optimized value, beyond which the melting rate kept approximately constant or slightly reduced.

With regards to porous matrix inserts, heat is predominantly conduction-driven transferred for the duration of melting due to their tiny pores and high thermal conductivity, where the pore size is always insensitive to melting rate enhancement. However, if the convection heat transfer is not negligible, an appropriate pore size should be sought in order to maximize the melting rate. Lafdi et al. [15] experimentally studied melting in a rectangular enclosure heated from the left side and reported that the heater surface temperature of low porosity foams (with same 10 PPI, pores per inch) can be comparatively lower than the higher porosity ones due to the greater conduction. For the same porosity, 93.7%, foams with larger pore sizes resulted in slightly lower heater surface temperature because of stronger convective heat transfer. The authors suggested to obtain an optimal value of porosity and pore size for maximum utilization of both conduction and convection effects. Sundarram et al. [16] performed simulations of PCM infiltrated microcellular metal foams where the pore size was less than 100 μm and investigated the effect of porosity and pore size on melting enhancement. The simulated results indicated that for a fixed porosity, a smaller pore size could lead to a lower temperature at the heat source for a longer period of time and the effect can be more pronounced at higher heat generation rate and lower conductive cooling conditions. Specifically, the net effective thermal conductivity of a PCM microcellular metal foam composite could be doubled by decreasing the pore size from 100 μm to 25 μm. Dinesh et al. [17] used a geometry creation model to investigate the effects of pore size variations/distributions (0.5 cm < r < 1.0 cm, 1.0 cm < r < 1.5 cm and 1.5 cm < r < 2.0 cm) on melting rate improvement by keeping the bulk porosity constant. The simulation results showed that the pore size distribution could strongly affect the melting rate. Moreover, it was reported that smaller pores resulted in faster melting and higher heat transfer rates for both low and high porosity systems, where cascaded porosity foam [18] may be an interestingly alternative solution. Parida et al. [19] further studied the effect of convection on melting enhancement, especially for different pore sizes. Three different pore size ranges (3-4 mm, 4-5 mm and 5-6 mm) were investigated for a constant porosity of 50%. The simulated results indicated that convection played a major role for larger pore size systems and the overall melting time reduced with increasing pore size at first and then decreased with further increased pore size due to the contribution of convective heat transfer.

While fins or foams offer benefits particular to their design, many novel PCM-based thermal enhancers in-between macroscopic fins and microscopic porous foams have been devised thanks to advances in additive manufacturing, for instance tree-like branching fins and periodic structures. Pizzolato et al. [20] designed high-conductivity fins for shell-and-tube TES units with a topology optimization approach. The simulated results showed that

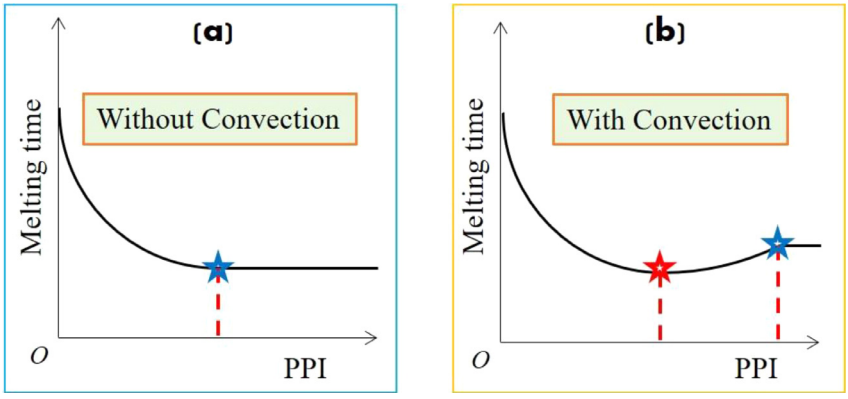

Fig. 1. Melting time variation versus PPI with or without natural convection.

melting and solidification could be enhanced remarkably through convection by employing well-engineered fins with specific design features while the optimized fin layouts for melting and solidification can be fundamentally different. Righetti et al. [21] conducted experiments for the melting intensification using 3D periodic structures with different cell size (10, 20 and 40 mm) under the same porosity. It was found that the 10 mm sample had the least charging time, compared to the other two. Opolot et al. [22] investigated the effects of wall thermal contact resistance for such geometry and offered theoretical and numerical results to evaluate and minimize the thermal contact resistance. Zhao et al. [23] numerically studied the effects of pore density of a 0.9 porosity periodic structure on the PCM melting time reduction for different ligament materials (copper, aluminium, nickel, and stainless steel). Two different trends of the melting time curves with respect to PPI, i.e., monotonical decline and parabolic, were reported depending on the material (enhancer) properties. The critical cell size with respect to melting time minimization were ascertained, and the critical value for stainless steel under considered settings was approximately 3-5 PPI, while it was 10 PPI for the copper periodic structure. Nevertheless, the underlying mechanism leading to the existence of a critical cell size has not been unveiled.

2. Critical cell size

With a certain porous foam, scholars tend to incorporate additional techniques, such as heat pipe [24] and nanoparticles [25], for further heat transfer augmentation. However, it makes perfect engineering sense to optimize a designed porous matrix instead of combining a sub-optimal design with an extra heat transfer enhancement system. Pizzolato et al. [26] developed a general mathematical framework for multi-scale topology optimization of multi-material structures that can be utilized for LHTES design. Using the framework, the authors obtained various optimized metal matrix and macroscopic fin layouts for single material constraint, and macroscopic and microscopic layouts of metal matrices configurations for multiple materials with controllable subdomains and structures. The main defect, however, is that effect of natural convection is not considered due to high computational cost, which can lead to a very different melting behaviour and performance [27,28]. In fact, irrespective of enhancer configurations, optimal fin spacing of straight fins, optimal pore size of porous matrices and critical cell size of periodic structures are all directed to the optimized distances between adjacent conducting pathways, where a climax of combined heat transfer rate for the entire period of melting can be realized by fine-tuning the interplay between conduction and convection heat transportation. The missing part in the literature is to identify pertinent parameters and investigate their impacts on the heat transfer performance so that an optimised system can be designed regardless of the enhancer and PCM material properties. Hence, this paper is presented to fill this gap using a previously developed periodic structure model [23].

Generally, as the cell size of the periodic structure reduces, the conduction effects are enhanced until reaching a critical value [29,30], beyond which conduction heat transfer is only marginally improved. This manifests in a melting time curve shown in Fig. 1(a) which is valid for a pure conduction heat transfer system. With most of the PCM systems, however, both natural convection and conduction heat transfer mechanisms are present. Convection heat transfer always loses ground in smaller cells partly because of reduced permeability. Moreover, a uniform cell temperature weakens natural convection in a cell which is driven by a local temperature (liquid density) difference. With larger less conductive cells, nonetheless, a more non-uniform temperature is anticipated, and a bigger mass of liquid gets to circulate and convect the heat across the cell. These trends are different from the one expected for a purely conducted system. Hence, incorporating both natural convection and conduction can result in a very different heat transfer trend depending on the cell size and conductivity of the thermal enhancer (cell walls). Basically, with increasing PPI, the curve of melting time can show a parabolic trough, followed by a plateau as schematically demonstrated in Fig. 1(b).

The relative significance of convection, compared to conduction, is crucial to the occurrence of two different melting time patterns. If natural convection is comparatively negligible, the critical PPI can be determined using Fig. 1(a). Otherwise, one can ascertain the critical PPI value by considering Fig. 1(b). Under such circumstances, a larger cell size (smaller PPI), relating to a lower manufacturing cost, can be obtained through the following strategies:

1) Improving convection. For an isothermally laterally heated PCM box, the length of PCM container matters. According to [31], the heat is mainly conducted into the PCM before the melt front reaches$HRa_H^{-1/4}$, thereafter, the melt front advance is dominantly by convection. This indicates that elongating enclosure length can be a good option, by which natural convection can account for more percentages to completely melt the PCM. Likewise, another possible way is to modify the orientation of the PCM tank.
2) Degrading conduction. Lowering the thermal conductivity of periodic structure ligaments that could lift the relative significance of convection, thus resulting in a smaller critical PPI.
3) Using both strategies. Increasing the porosity impairs conduction by reducing extended surface area, meanwhile, it can also slightly enhance convection due to thinner obstacles for liquid currents.

Table 1
Thermophysical properties of the considered PCM and periodic structure materials [23].

	PCM	Cu	Al	Ni	SS
Density ρ (kg/m^3)	860	8978	2719	8900	8030
Thermal conductivity k (W/m·K)	0.2	387.6	202.4	91	16.27
Specific heat c_p (J/kg·K)	2000	381	871	460.6	502.48
Thermal expansion coefficient β (1/K)	0.001				
Dynamic viscosity μ (Pa·s)	0.03499				
Melting point T_m (K)	354.15				
Latent heat L (J/kg)	176000				

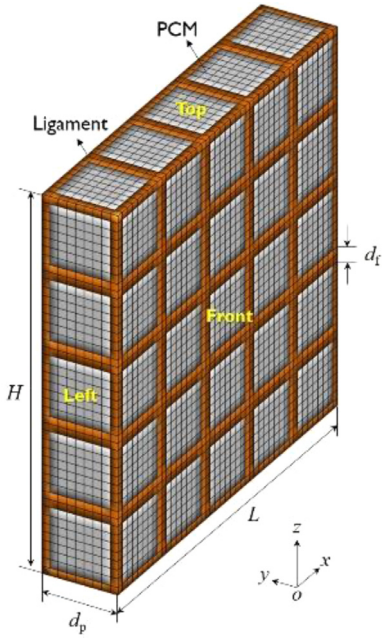

Fig. 2. Schematic of the computational domain for the physical model [23].

Moreover, altering thermal boundaries (e.g. increasing wall temperature), can upgrade conduction and convection, thus, leading to a uniformly valid critical cell size of the periodic structure for given cells. Therefore, in the present study, critical cell sizes under different periodic structure properties (thermal conductivity and porosity) are numerically ascertained. Then, effects of enclosure parameters and thermal boundaries on shifting values of critical cell size are investigated. Our investigation led to observation of a scatted melt front for some cases which is different from a continuous one reported in the literature. We observe that for given combination of materials and cell sizes, the PCM can be locally melted before the moving melt front reaches that spot. This has not been publicly reported before and we present a theoretically-driven criterion for occurrence of localized melting in presence of periodic structures.

3. Problem description

3.1. Physical model

The considered physical model has dimensions of $H \times L \times d_p$, where $H = L = 25.4$ mm, as shown in Fig. 2. The periodic structure metal wire net has been uniformly embedded in the PCM, which is used as a thermal enhancer for augmenting the PCM melting/solidification rate. RT-82 is adopted as the PCM while different materials for the periodic structure are considered here being: copper, aluminum, nickel, and stainless steel, with the thermophysical properties listed in Table 1. As seen, stainless-steel offers the lowest thermal conducitivy among the four materials considered here. However, it is resistant to corrosion (when submerged in a salt tank for high temperature thermal energy storage) and can work at such high tempertures (around 800 K) without suffering from creep unlike other metals considered in Table 1. Despite the low condcutivity value, a SS periodic structure still spreads the heat and breaks the PCM into smaller volumes which will melt faster. The choice of SS for a high tmeperature application is justified considering a balance between longevity, cost, safety, and fast reponse for a storage tank in a concentrating solar thermal (CST) plant [32].

As illustrated in Fig. 2, there are three geometrical parameters to describe the periodic structure: porosity (ε), ligament thickness (d_f), and cell diameter (d_p). To facilitate simulations, the cross-section of the ligament is considered as a square. Therefore, the relative porosity of this periodic structure is approximated as

$$1-\varepsilon = 3\left(\frac{d_f}{d_p}\right)^2 - 2\left(\frac{d_f}{d_p}\right)^3 \tag{1}$$

where the second term in the right-hand side is used to eliminate the overestimation of intersections. As seen, for the considered periodic structure, the three above-mentioned geometrical parameters are interdependent.

3.2. Governing equations

In order to simplify the numerical simulation, one can assume that the melted PCM motion across the periodic structure is incompressible laminar flow due to buoyancy-induced natural convection, where the density variation is modelled using the Boussinesq approximation. The governing equations using the enthalpy-porosity technique that account for conservations of mass, momentum (***x***, ***y*** and ***z*** directions) and thermal energy of the PCM can be expressed as

$$\frac{\partial u}{\partial x} + \frac{\partial v}{\partial y} + \frac{\partial w}{\partial z} = 0 \tag{2}$$

$$\rho\left(\frac{\partial u}{\partial t} + u\frac{\partial u}{\partial x} + v\frac{\partial u}{\partial y} + w\frac{\partial u}{\partial z}\right) = \mu\left(\frac{\partial^2 u}{\partial x^2} + \frac{\partial^2 u}{\partial y^2} + \frac{\partial^2 u}{\partial z^2}\right) - \frac{\partial P}{\partial x} - A\frac{(1-\gamma)^2}{\gamma^3+\sigma}u \tag{3}$$

$$\rho\left(\frac{\partial v}{\partial t} + u\frac{\partial v}{\partial x} + v\frac{\partial v}{\partial y} + w\frac{\partial v}{\partial z}\right) = \mu\left(\frac{\partial^2 v}{\partial x^2} + \frac{\partial^2 v}{\partial y^2} + \frac{\partial^2 v}{\partial z^2}\right) - \frac{\partial P}{\partial y} - A\frac{(1-\gamma)^2}{\gamma^3+\sigma}v \tag{4}$$

$$\rho\left(\frac{\partial w}{\partial t} + u\frac{\partial w}{\partial x} + v\frac{\partial w}{\partial y} + w\frac{\partial w}{\partial z}\right) = \mu\left(\frac{\partial^2 w}{\partial x^2} + \frac{\partial^2 w}{\partial y^2} + \frac{\partial^2 w}{\partial z^2}\right) - \frac{\partial P}{\partial z} - A\frac{(1-\gamma)^2}{\gamma^3+\sigma}w$$

$$+\rho g\beta(T-T_{\mathrm{ref}}) \tag{5}$$

$$\rho\left(\frac{\partial h}{\partial t}+u\frac{\partial h}{\partial x}+v\frac{\partial h}{\partial y}+w\frac{\partial h}{\partial z}\right)=k\left(\frac{\partial^2 T}{\partial x^2}+\frac{\partial^2 T}{\partial y^2}+\frac{\partial^2 T}{\partial z^2}\right) \tag{6}$$

where ***u***, ***v***, and ***w*** are superficial velocities in ***x***, ***y*** and ***z*** directions, respectively, which can be calculated from $(u,v,w)_{\mathrm{superficial}}=\gamma(u,v,w)_{\mathrm{actual}}$. "$\gamma$" denotes the liquid fraction in a numerical element that can be expressed as

$$\gamma=\begin{cases}0, & T\le T_{\mathrm{s}}(\text{solid phase})\\ (T-T_{\mathrm{s}})/(T_{\mathrm{l}}-T_{\mathrm{s}}), & T_{\mathrm{s}}<T<T_{\mathrm{l}}\ (\text{mushy zone})\\ 1, & T\ge T_{\mathrm{l}}(\text{liquid phase})\end{cases} \tag{7}$$

where T_{s} and T_{l} are solidus and liquidus temperature, respectively. The third term at the right-hand side of Eqns.(3)-(5), the Carman-Koseny term, is adopted as a momentum sink at the mushy region following Ref. [33]. σ is a small number (here equal to 0.001) to prevent division by zero. A is the mushy zone constant to describe the damping rate of the morphology of mushy zone. A proper value should be chosen [34,35] and this paper adopts 10^5 kg/(m^3·s) similar to Ref. [23].

In Eq. (6), "h" is the specific enthalpy defined as the sum of the sensible and latent heat:

$$h=h_{\mathrm{ref}}+c_{\mathrm{p}}(T-T_{\mathrm{ref}})+\gamma h_{sf} \tag{8}$$

where the h_{ref} is the reference enthalpy at the reference temperature T_{ref} (300.15 K).

For the metallic struts of the periodic structures, the thermal energy equation is

$$\frac{\partial T}{\partial t}=\alpha\left(\frac{\partial^2 T}{\partial x^2}+\frac{\partial^2 T}{\partial y^2}+\frac{\partial^2 T}{\partial z^2}\right) \tag{9}$$

3.3. Boundary conditions

Initially, the solid PCM composite is kept at a constant and uniform temperature (300.15 K). The left wall temperature remains constant and uniform (363.15 K) while the top, bottom, and right walls are adiabatic and the front and back planes are modelled as symmetry planes.

3.4. Numerical details

Numerical simulations in the present study are conducted using a commercially available computational fluid dynamics (CFD) software package, FLUENT 19.2. The governing equations are discretised by the finite volume method with a 3D double precision solver. The SIMPLE algorithm is used for pressure-velocity coupling while the PRESTO! scheme is implemented for pressure correction. A fully implicit scheme is used for transient terms while the convective terms are linearized using the QUICK-type scheme and the second order central differencing scheme is used to approximate the diffusive terms.

Numerical grids are produced by the ICEM software. Here, the 46k grids system with 0.2 s time step size are used in this study based on the independence analysis of grid resolution (46k, 190k, and 1597k) and time step size (0.1 s, 0.2 s, and 0.3 s). The current numerical model of periodic structures embedded in the PCM has been successfully validated in Ref. [23].

4. Results and discussion

4.1. Effect of periodic structure properties

As described, for the same PCM, ligament material properties and porosities of the periodic structures could affect the critical PPI. Hence, for a fixed (0.75) porosity, different ligament materials (copper, aluminium, nickel, and stainless steel) with thermal-diffusivity-ratios ($\alpha_{\mathrm{ligament}}/\alpha_{\mathrm{PCM}}$= 974.5, 735, 190.9 and 34.7) are studied for four different cell sizes (PPI = 3, 5, 7 and 10). Keeping the PCM-periodic structure enclosure identical, three more porosity values (ε = 0.8, 0.85 and 0.95) of periodic structures are then extensively examined.

4.1.1. Liquid fraction

The temporal variations of liquid phase fraction of 0.75, 0.8, 0.85 and 0.95 porosity for different PPIs and ligament materials during melting are displayed in Fig. 3(a)-(d), respectively.

For the rows in Fig. 3, such as (a) for 0.75 porosity, the effect of PPI has been reported in four subfigures regarding different ligament materials. In the Cu subfigure, the melting rate elevates as the value of PPI increases from 3 to 10 and different PPI curves are distinguishable. As thermal-diffusivity-ratio ($\alpha_{\mathrm{ligament}}/\alpha_{\mathrm{PCM}}$) falls, all curves are progressively bundled, where curves of PPI = 5, 7 and 10 are well-agreed in the Ni subfigure and all curves converged for stainless-steel cases. The underlying mechanism relates to the interplay between weakened convection and intensified conduction, as the cell size of the periodic structure diminishes (PPI increases). Once the PPI is fixed, as the thermal-diffusivity-ratio reduces, the convection strength remains unchangeable while the conduction capability is weakened. For the copper-based periodic structure of all PPIs, the confined PCM is seemingly conduction-like melted for the entire melting duration. This means a larger PPI is preferred for a quicker melting rate (see Fig. 1(a)). As the $\alpha_{\mathrm{ligament}}/\alpha_{\mathrm{PCM}}$ contracts, the conduction heat transfer ability worsens, and the invariant convection significantly stands out. Therefore, for a low thermal-diffusivity-ratio PCM-periodic structure system, different PPI curves are unified, and one needs to seek an appropriate PPI to achieve the highest combined heat transfer rate (see Fig. 1(b)). A similar phenomenon has been detected in other rows in Fig. 3(b)-(d) for different porosities.

For each column of Fig. 3, using the same material, the porosity is only variable, which increases from 0.75 to 0.95 downwards. Generally, increasing the porosity of a periodic structure (fixing material and PPI) enfeebles the conduction due to the reduced heat transfer surface area with thinner ligaments, meanwhile, the convective heat transport capability gets strengthened, owing to slightly enlarged permeability. As such, for each column, different PPI curves gradually converge as the porosity increases and the phenomenon becomes more profound for inferior thermal diffusivity materials, e.g., nickel. By contrast, stainless-steel figures exhibit an opposite tendency: instead of convergence, curves are increasingly diverging at the large liquid fraction portion as the porosity surges. This indicates that, for the entire duration of melting within the stainless-steel periodic structures, a lower PPI is preferred since convection heat transfer is comparably dominant.

One explicit finding is that higher PPIs always lead to a shorter melting time for copper structures despite of porosities; for the stainless-steel periodic structure, it is insensitive to PPI for the low (0.75) porosity while lower PPIs are more effective when the porosity is high.

4.1.2. Melting time

For the same mass of PCM, the melting time when the PCM completely melted can be used to fairly assess the averaged melting rate. For the studied cases, the mass of PCM are different for various porosity but, for the same porosity, one can confidently compare the melting time in terms of different PPIs. Note that the melting time of pure PCM without any inserts (100% porosity or PPI = 0) is around 10k second [23]. Fig. 4 shows the melting times in terms of PPI for different periodic structure materials under different porosities.

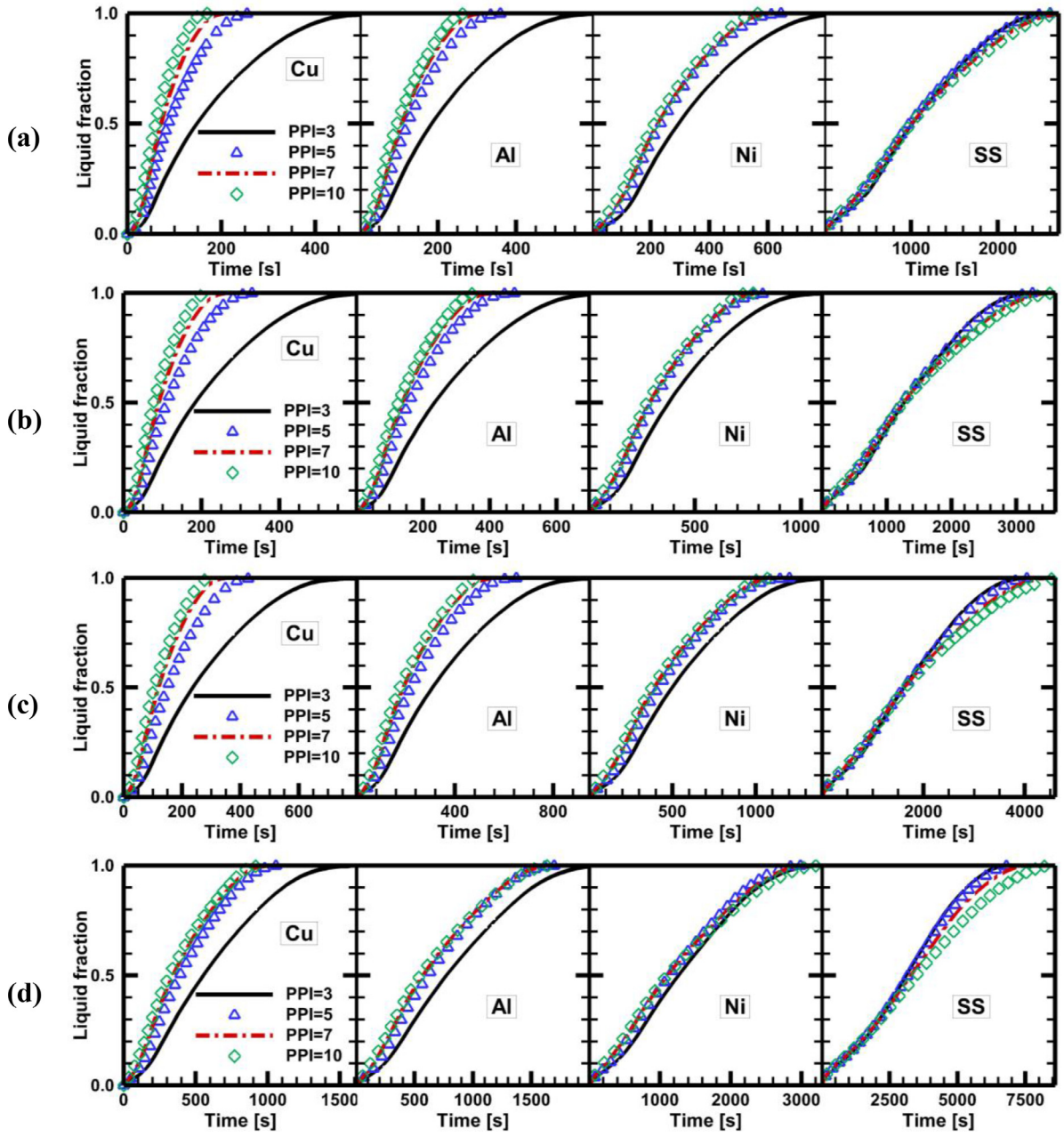

Fig. 3. Liquid fraction evolutions for different ligament materials under various porosities (a) 0.75; (b) 0.8; (c) 0.85 and (d) 0.95.

As seen in Fig. 4, the monotonical decline trend (see Fig. 1(a)) is found for copper- and aluminium-based periodic structures, for different porosities. One finds that, for 0.95 porosity aluminium periodic structure, PPI=7 and 10 scenarios have almost identical melting times (horizontal red dot-dash line), indicating the natural convection starts to be significant and the improved conduction capability is nearly equivalent to the devitalized convection. One predicts the curve of 0.95 porosity becomes parabolic (see Fig. 1(b)) if the thermal-diffusivity-ratio continues to drop, and it is validated by the nickel structure results, where 5 PPI is the best scenario with 2956 s.

Distinguishably, for the stainless-steel periodic structures, the melting time curves for all porosity sizes display a parabolic trend. The underlying reason for such a phenomenon is associated with the limited conducting enhancement due to the low thermal-diffusivity-ratio of stainless steel. Herein, a lower PPI (larger cell size) can be beneficial on reducing the melting time by taking advantage of convective heat transport.

To summarize, one observes that higher porosity prolongs the melting period, but the extension time ratio is not the same when the thermal-diffusivity-ratio reduces (Cu to SS). More importantly, Fig. 5 shows the critical PPI as a function of porosity and thermal-diffusivity-ratio for the considered enclosure. As seen, for copper- and aluminium-made periodic structures, the critical PPI is equal to (or larger than) 10 for 0.75 to 0.95 porosities. As for nickel periodic structures, the optimal PPI is still 10 for 0.75, 0.8 and 0.85 porosities, however, the value reduces to 5 PPI for the 0.95 porosity scenario. For SS, the critical PPI of 0.75 porosity is 5 while it reduces to 3 PPI (or less) for a higher porosity. Overall, increasing porosity or lessening thermal diffusivity of the periodic structure could lead to a lower critical PPI.

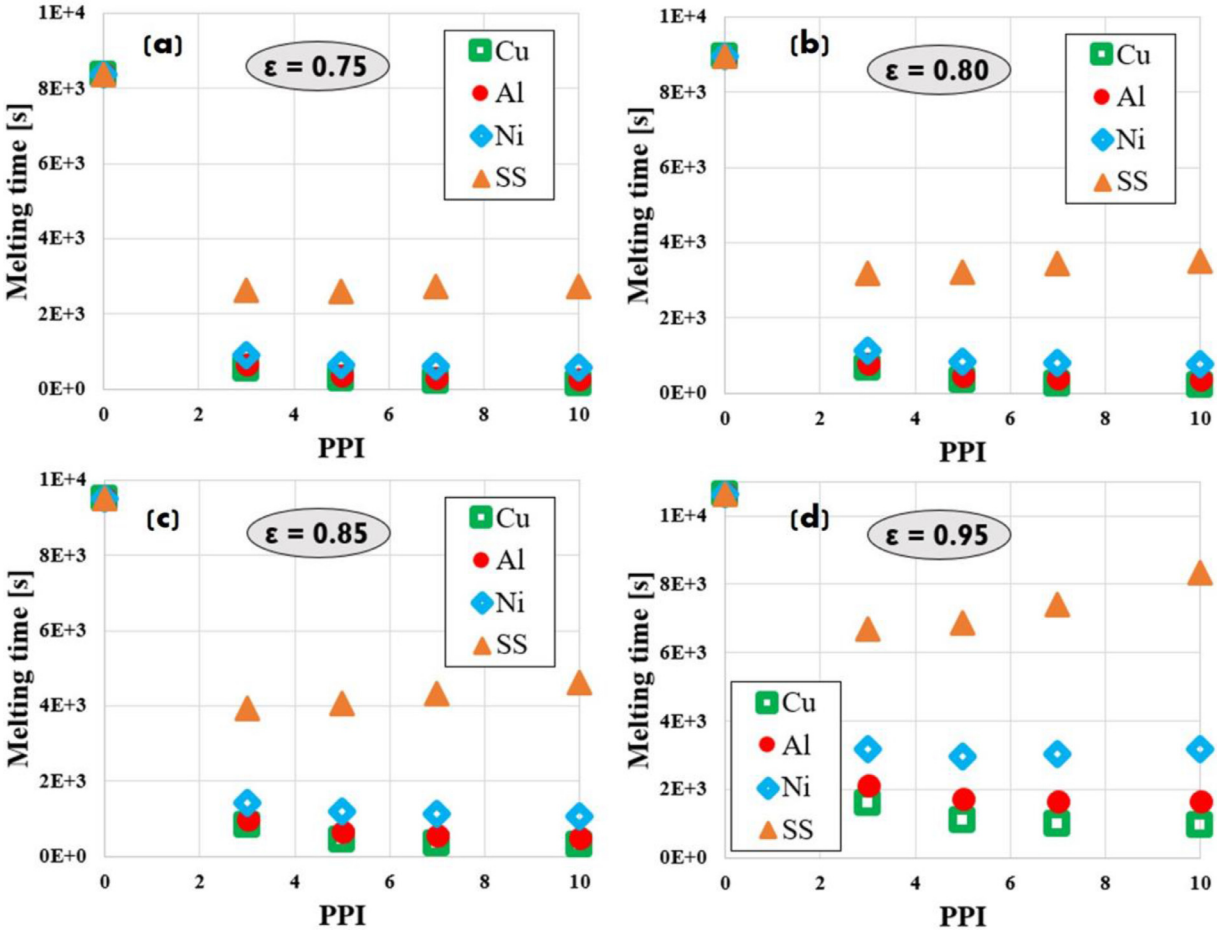

Fig. 4. The melting times versus PPI for different ligament materials for different porosities (a) 0.75; (b) 0.8; (c) 0.85 and (d) 0.95.

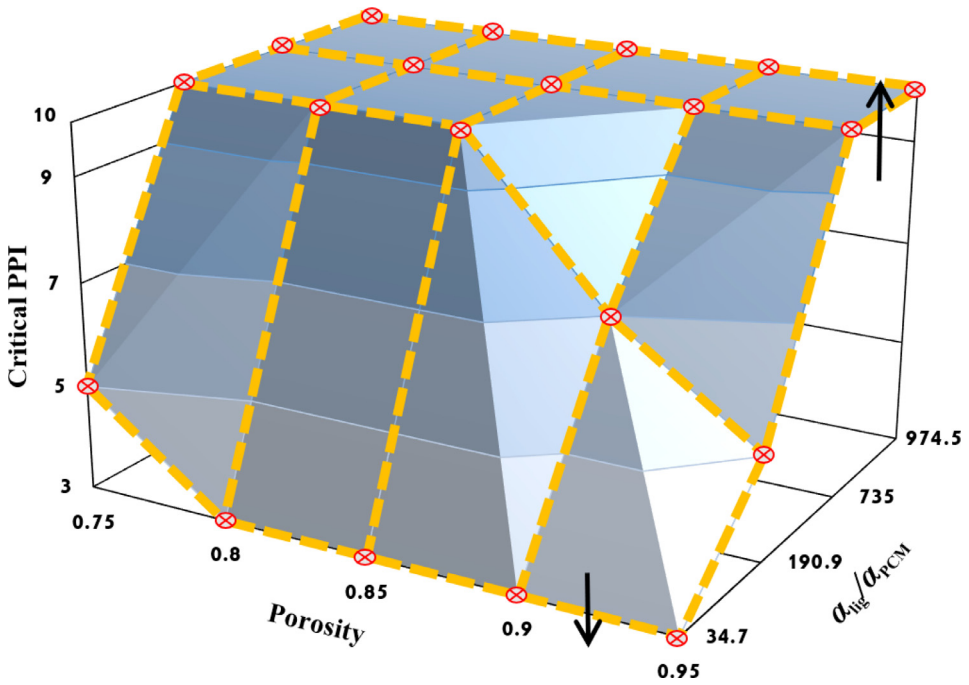

Fig. 5. Critical PPI as a function of porosity and thermal-diffusivity-ratio.

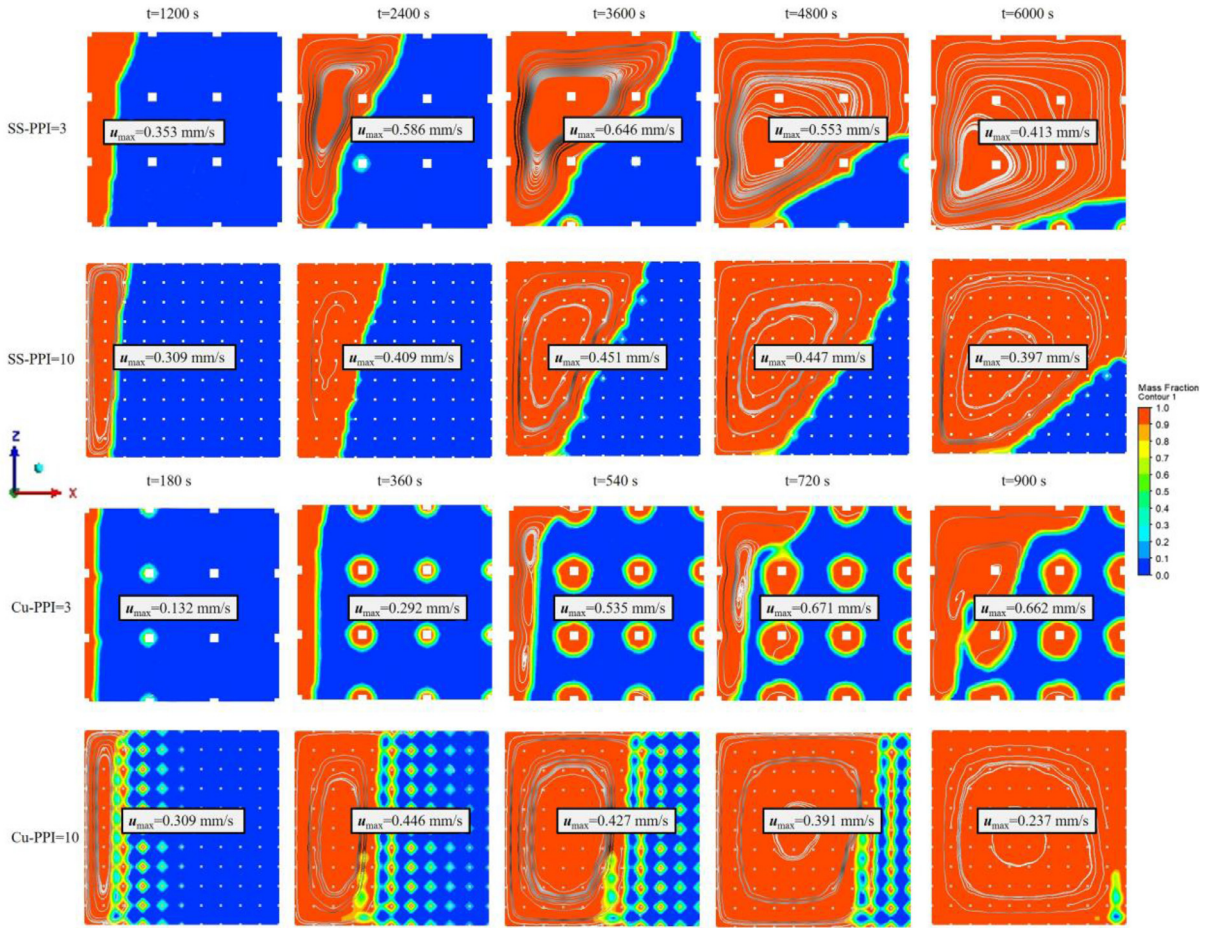

Fig. 6. Liquid fraction contours with streamlines and maximum velocities of PPI=3 and 10 under 0.95 porosity cases made of stainless steel (upper two rows) and copper (lower two rows) for different time instants.

4.1.3. Localized melting

To further understand the impacts of cell size (PPI) and the thermal-diffusivity-ratio on melting rate enhancement, liquid fraction contours of 0.95 porosity periodic structures on the mid-XZ plane are displayed in Fig. 6 for various time instants.

The first two rows are stainless steel periodic structures for PPI =3 and 10 at 1200 s, 2400 s, 3600 s, 4800 s, and 6000 s, respectively. As shown, only one convective roll appears during the process and the melt layer advances in the transverse direction, closely similar to pure PCM melting behaviours for the 10 PPI case. Localised melted PCM adjacent to the ligament that is right to the melt front can be found in the 3 PPI case as the time progresses. However, the localised melting (LM) phenomenon is just visually observed and a possible appropriate definition of its occurrence is that the heat spreads through the periodic structure network quickly enough, so that there exists, at least, a periodic structure position, where the temperature equals to melting point, is ahead of the primary melt front at any instant during the entire melting process.

The definition designates that the thermal-diffusivity-ratio is a key parameter. From the viewpoint of heat transfer, two kinds of melting behaviours can be found: if the thermal-diffusivity-ratio is very low ($\alpha_{\text{ligament}}/\alpha_{\text{PCM}} \to 1$), melting happens in stages (similar to pure PCM [31]). On the other extreme, however, when the ratio is sufficiently high ($\alpha_{\text{ligament}}/\alpha_{\text{PCM}} \to +\infty$), the temperature of entire periodic structure immediately rises up to that of the wall and the PCM is anticipated to melt uniformly and simultaneously across the whole region. Nonetheless, the diffusivity ratio falls between these two extremes and one can expect localized melting. That is, the PCM can be melted, at the ligaments, away from the heated wall and before the melting front reaches them. Hence, the liquid fraction contours show non-zero values as patchy spots or islands surrounded by solid PCMs while a melting front originating from the heated wall approaches them. While this phenomenon, localized melting, has been observed experimentally, there is no criterion to predict its occurrence for a period structure. Hence, we offer a simple model based on two distinct time scales. One is for the heat to diffuse through the storage tank and the other one is for a volume of PCM to melt. The former can be shown to follow

$$t_1 \sim L^2/\alpha_{\text{ligament}} \tag{10}$$

This is the time it takes for heat to diffuse from the heated wall, making a pass to the other end of the tank (L) after increasing the ligament temperature. Note that heat can be diffused through either the ligaments or the PCM but as the ligaments offer a much lower thermal resistance, the time scale for diffusion through ligaments is shorter compared with that of the PCM. If this time scale is shorter than that of melting front movement, then localized melting (at the vicinity of the ligaments understandably) is anticipated.

The second time scale is defined as that of melt front movement. For us to ascertain that, we need to follow the heat path from the wall. The PCM is now divided to smaller volumes filling cells. Melt front is formed when a cell parallel to the heated wall is melted. The time it takes for heat to melt this cell volume is approximated as the time heat is diffused in the whole cell bringing

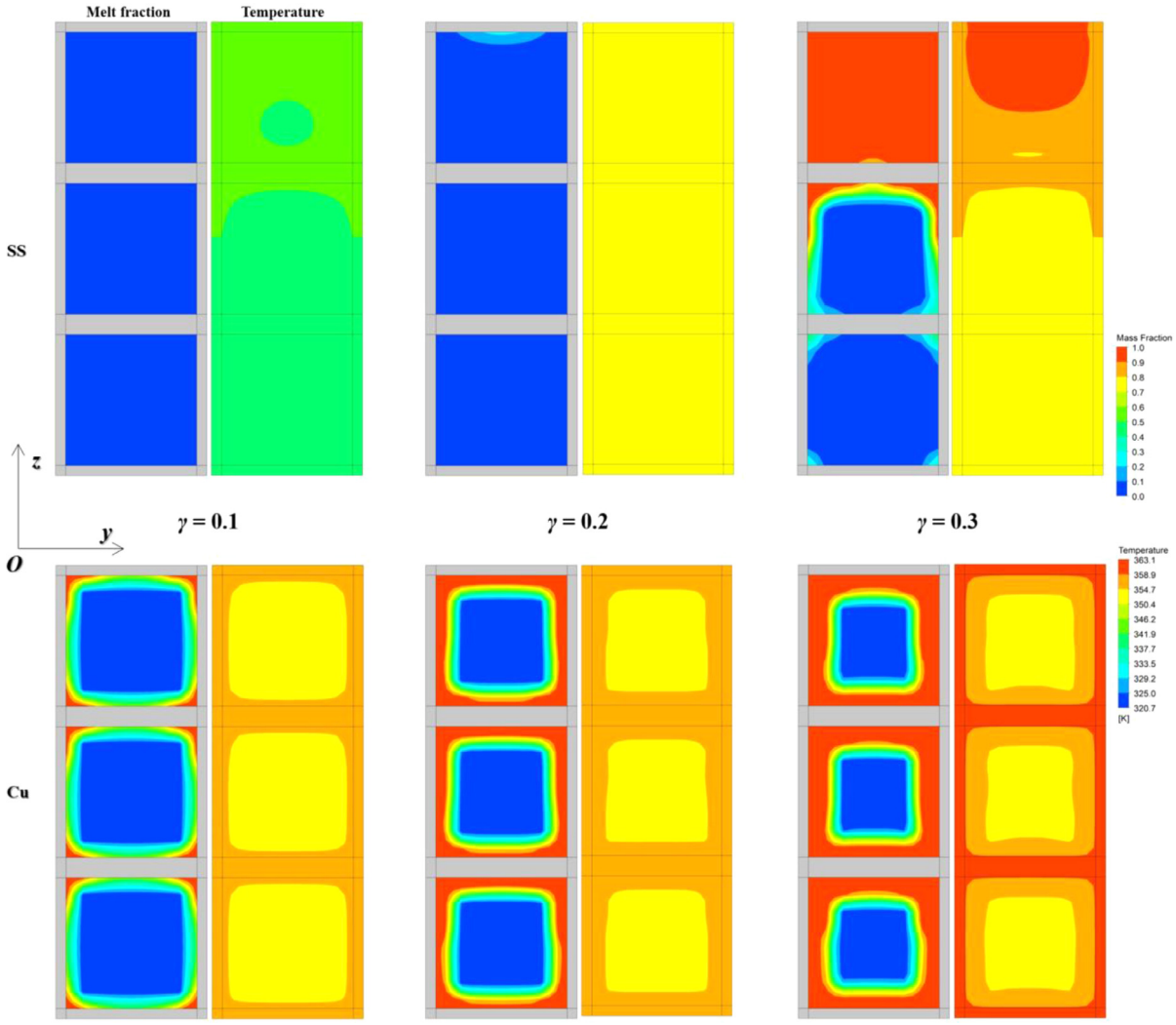

Fig. 7. Melt fraction (left) and temperature (right) contours of the YZ plane at $x = 8.47$ mm when liquid fraction equals to 0.1, 0.2 and 0.3 for stainless-steel (top) and copper (bottom) periodic structures of 0.95 porosity and PPI = 3.

it to a higher (melting) temperature. This diffusion time is given by

$$t_2 \sim d_p^2/\alpha_{PCM} \tag{11}$$

These two time scales show a comparison between heat transfer across the ligaments and melting at the heated wall; hence the ratio

$$t_1/t_2 < 1 \tag{12}$$

which can indicate that heat penetration through the ligaments is faster than melting within a cell; hence localized melting. The above can be rearranged to read

$$LM \text{ may occur when } \phi = \frac{d_p}{L}\sqrt{\frac{\alpha_{ligament}}{\alpha_{PCM}}} > 1 \tag{13}$$

As expected, for stainless-steel periodic structures, the ϕ values of 3 PPI and 10 PPI scenarios are 1.96 and 0.59, respectively, which are consistent with the aforementioned observation.

For the two rows in the bottom of Fig. 6, the liquid fraction contours of the copper periodic structure cases with streamlines and maximum velocities are presented. More profound localised melting is found for five different time instants, say 180 s, 360 s, 540 s, 720 s, and 900 s, owing to the very short thermal response time of the periodic structure. Note that the local melted PCM size almost stops enlarging after 720 s while the volume of left melted PCMs keeps increasing. This phenomenon can be explained that, for localised melting, conduction is the dominant heat transfer mechanism, owing to lower temperature difference and small localised cavity size, while the convective heat transfer at the left main melted region can be relatively prevalent as melted PCM puddles merged. Table 2 shows the localised melting (LM) with respect to thermal-diffusivity-ratio ($\alpha_{ligament}/\alpha_{PCM}$) and ϕ for different materials.

Table 2
Localised melting (LM) with respect to $\alpha_{ligament}/\alpha_{PCM}$ and ϕ for different materials.

Material		SS	Ni	Al	Cu
$\alpha_{ligament}/\alpha_{PCM}$		34.7	190.9	735	974.5
3 PPI	ϕ	1.96	4.61	9.04	10.41
	LM	Yes	Yes	Yes	Yes
10 PPI	ϕ	**0.59**	1.38	2.71	3.12
	LM	**No**	Yes	Yes	Yes

For the 0.95 porosity 3 PPI periodic structures made of stainless steel and copper, Fig. 7 illustrates the melt fraction and temperature field contours of the YZ plane at $x = 8.47$ mm for liquid fraction equals to 0.1, 0.2 and 0.3. Similar to Fig. 6, one could de-

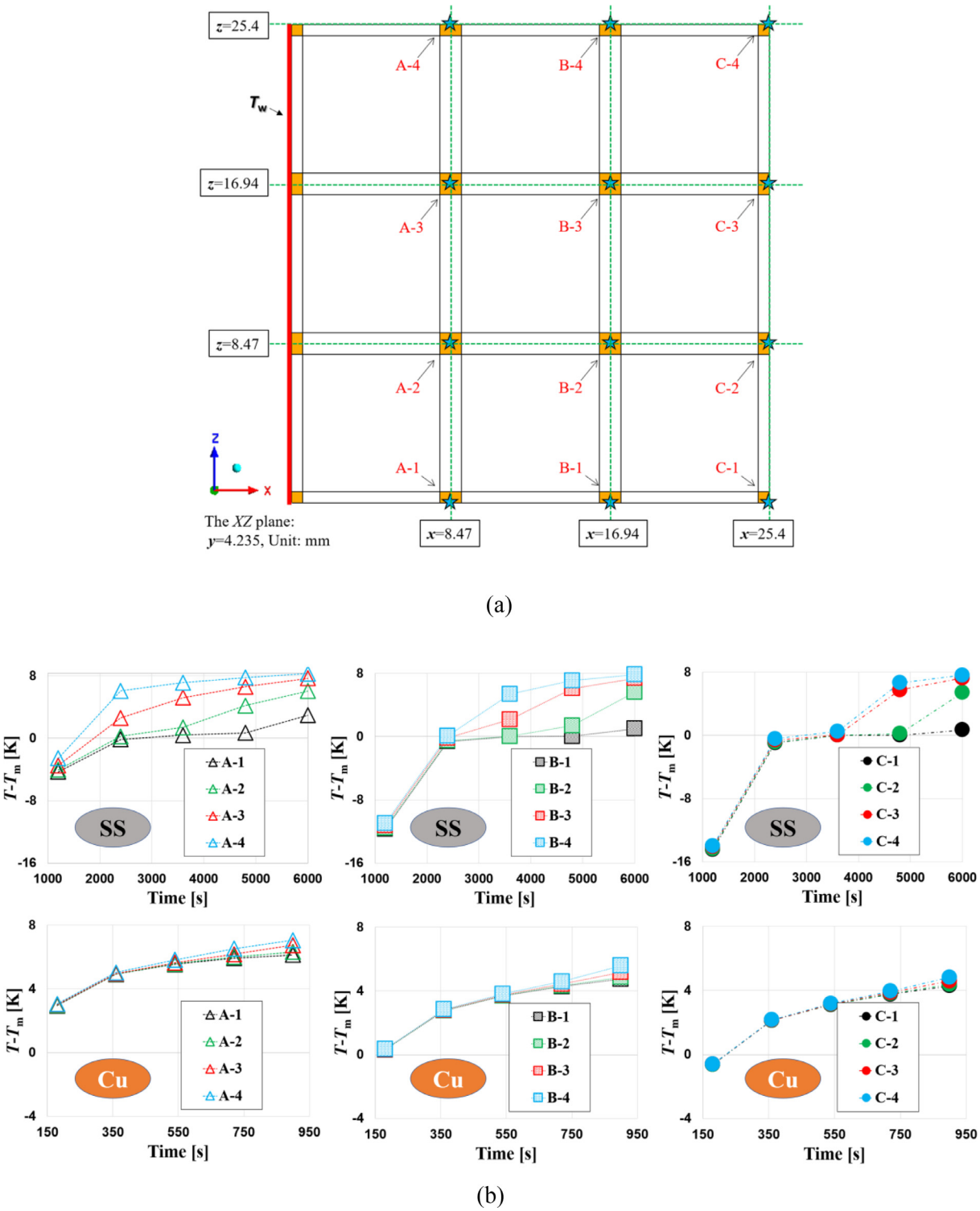

Fig. 8. Schematic of ligament positions of periodic structures under 0.95 porosity and 3 PPI (a) and their temperature evolutions (b) for stainless steel (the upper row) and copper (the lower row) materials.

tect the localised melting in the copper periodic structure for different liquid fraction values, which is absent in the stainless-steel case. On the other hand, a high local temperature difference between ligament and PCM is found in the copper periodic structure case, while local thermal equilibrium is found in the stainless-steel case.

To further demonstrate localised melting, the ligament temperature should be examined. Herein, different ligament locations within the mid-XZ plane, corresponds to Fig. 5, of 0.95 porosity and 3 PPI periodic structures are schematically presented in Fig. 8(a). As seen, A-1, A-2, A-3 and A-4 are located at the first column from bottom to the top. Likewise, the second column uses B-1, B-2, B-3 and B-4 while C-1, C-2, C-3 and C-4 are within the third column. Temperature difference (ΔT=T-T_m) evolutions of these measurement points are displayed in Fig. 8(b) for stainless steel and copper, respectively.

For the stainless-steel (the upper row of Fig. 8(b)), one observes that: 1) the divergence of curves emerges once the ligament exceeds the melting temperature and, for the same column, the temperature of higher position is higher, indicating the significant upwards convection. The underlying mechanism is that the hotter melted PCM moves up to the top, narrowing down the temperature difference between the ligament and liquid phase PCM at higher positions. This will deteriorate the local heat exchange rate and thus lead to more thermal energy accumulating in the local ligament, resulting in a higher temperature. 2) Before melting, curves of second (B) and third (C) columns converge well. This means that there is a uniform thermal penetration rate in the horizontal direction through the ligament network, despite of the non-parallel melt front. 3) The T-T_m values of A-1, B-1 and C-1 are very close to zero for the entire duration of melting, which reflects the existence of a time-consuming "shrinking solid" regime which cannot be eradicated with the presence of stainless-steel periodic structures.

As for copper, in the lower row of Fig. 8(b), the pattern of curves differs. First, curves of three columns agree with each other comparably well during melting, especially for the third one (C-1 to C-4), which indicates the absence of convection nearby. This corresponds well with the equivalent melted PCM cavity size near the ligaments of the third column, shown in Fig. 6. A detailed look reveals that curves of A-1 to A-4 diverge apparently after 720 s, as well as B-1 to B-4 curves, which indicates that, in the main liquid phase PCM reservoir, convection heat transfer still accounts for some weights. Second, most temperature differences of three columns are higher than zero, which correspond to localised melting.

4.2. Effect of tank parameters

Upon the completion of determining critical cell size for various periodic structure properties within a fixed container, the cell size value could be modified by manipulating tank parameters. Hence, the enclosure length and orientation are then further investigated.

4.2.1. Enclosure length

The enclosure length is another vital parameter for a laterally heated PCM box. As the enclosure elongated, more percentages of PCM lie in the convection-dominant region and the critical cell size enlarges. In this section, based on 0.95 porosity copper periodic structures, more numerical cases of enclosures with doubled and tripled lengths, respectively, are computed. Fig. 9 shows the melting times divided by n with respect to PPI, where the enclosure possesses the length of nL (n = 1, 2 and 3).

Trends of melting time curves evolve as the enclosure length increases, in detail, from monotonical decline to the parabolic trend. Note that, as the enclosure length further increases, it seemingly converts to monotonical increase while, in fact, it is still the parabolic trend since the melting time of pure PCM (PPI approaches zero) is much higher. The melting times for PPI of 3, 5, 7 and 10 are 3482.2 s, **3195.6 s**, 3298.8 s and, 3370.2 s, respectively, for the 2L-enclosure and 6270.8 s, 6544.6 s, 7109 s and 7375 s, respectively, for the 3L-enclosure. Hence, the critical cell sizes of the 0.95 porosity copper periodic structures are 10 PPI for the L-enclosure, 5 PPI for the 2L-enclosure and 3 PPI (or less) for the 3L-enclosure, which corroborates again that a longer enclosure leads to a lower critical PPI (or a larger critical cell size).

Furthermore, the liquid fraction contours of 0.95 porosity copper periodic structures with 2L in length on the mid-XZ plane for PPI = 3 and 10, respectively, at 720 s, 1440 s, 2160 s, and 2880 s are exhibited in Fig. 10. For 3 PPI showed in the left column of Fig. 10, the primary liquid PCM reservoir affected by the left heated wall indicates the presence of natural convection as the top portion of liquid-solid interface melts faster at 720 s. The localised melted PCMs that is adjacent to local ligaments are found and sizes of those independent melted PCMs are diminished along the x direction resulting from the decreased ligament temperature. As the melting progresses, the convective roll enlarges with merging localised melted PCM reservoirs and the convective heat transfer contribution becomes more significant. One could find that the curvature of the melt front of the primary melted PCM reservoir is comparably distorted due to the emergence of localised melted PCMs.

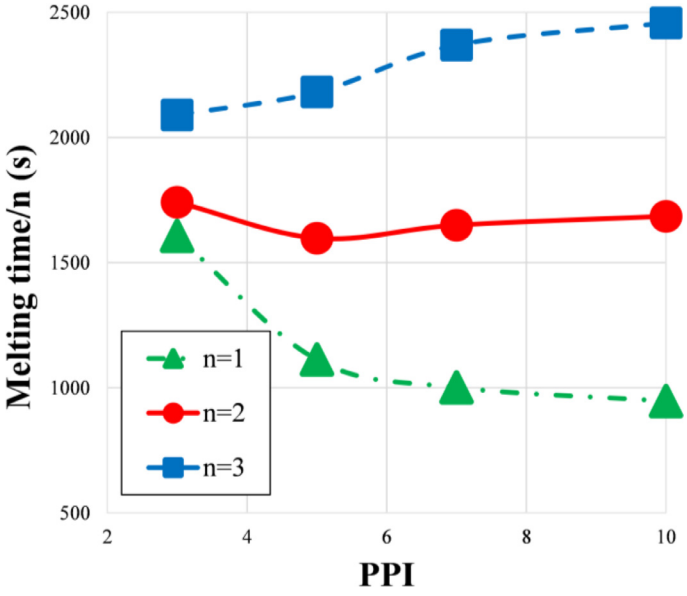

Fig. 9. Melting time over n versus PPI for a computational size with nL length (n = 1, 2 and 3) of 0.95 porosity copper periodic structures.

By contrast, the right half of Fig. 10 demonstrates the melt front advances and streamlines of melted PCMs for the 10 PPI case. It is found that the solid-liquid interface is nearly straight and parallel at 720 s and its top part just melts quicker slightly as time progresses. Compared to PPI = 3, the melt fronts are smoother but blurred.

4.2.2. Enclosure orientation

As aforementioned, adding weights of convective heat transfer can lower the critical PPI. The effect of enclosure orientation is subsequently examined since it also modifies the strength of natural convection. For the 0.95 porosity copper periodic structure, top and basal heating with the same wall temperature were implemented. The top heating scenario undoubtedly has the weakest (nearly zero) strength of natural convection due to thermal stratification. Basal heating owns the strongest natural convection since it doesn't have the "shrinking solid" regime [31], compared to the lateral heating. The time scale of the "shrinking solid" regime accounts for approximate $1/(1+l/L)$[27] in comparison with the complete melting time, where "l" is the length of the remaining PCM solid. One can estimate that, for a same PCM enclosure, the melting time of lateral heating is about two times longer than that of basal heating, which has been experimentally validated by Kamkari et al. [36].

Fig. 11 displayed the melting time versus PPI for top, lateral, and basal heating. One observes a trend of monotonical decline for all three curves. These curves merge well once PPI > 7, which indicates the natural convection within the entire enclosure is inhibited. Quantitively, the melting times of PPI = 3, 5, 7 and 10 are 1776 s, 1196.6 s, 1026.4 s and 939 s, respectively, for top heating, while the values are 1395 s, 1052.2 s, 1006.8 s and 931.6 s, re-

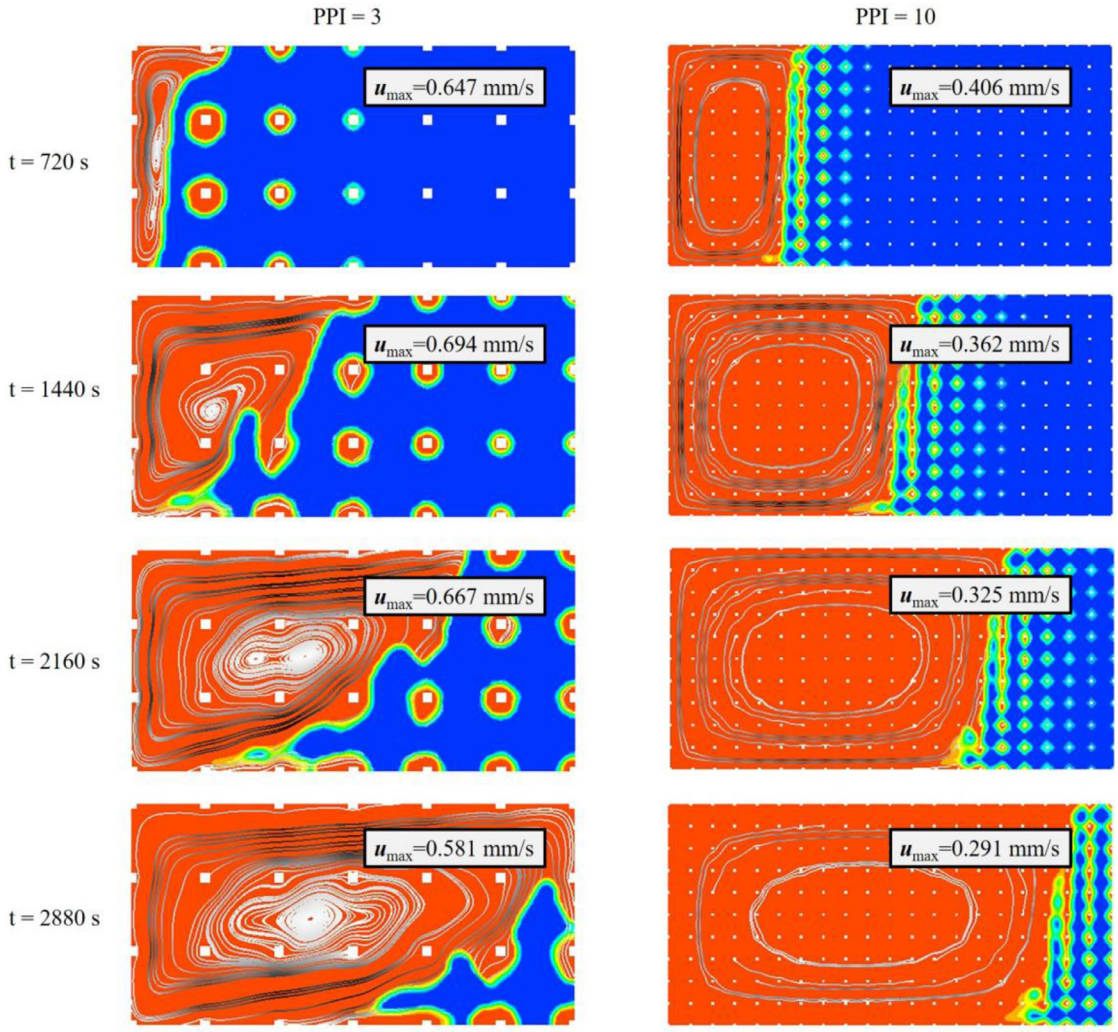

Fig. 10. Liquid fraction contours with streamlines and maximum velocities of PPI = 3 (left) and 10 (right) for the 0.95 porosity copper periodic structures with 2*L* in length for different time instants.

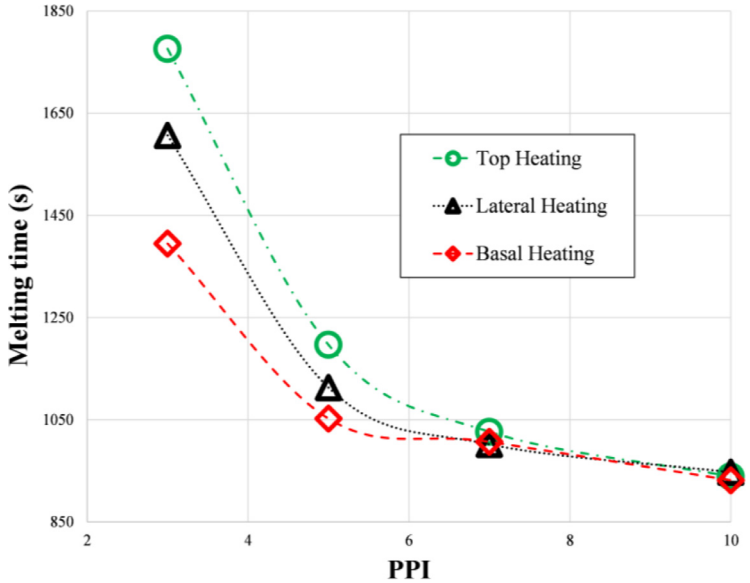

Fig. 11. The melting time versus PPI for different orientation heating of 0.95 porosity copper periodic structures.

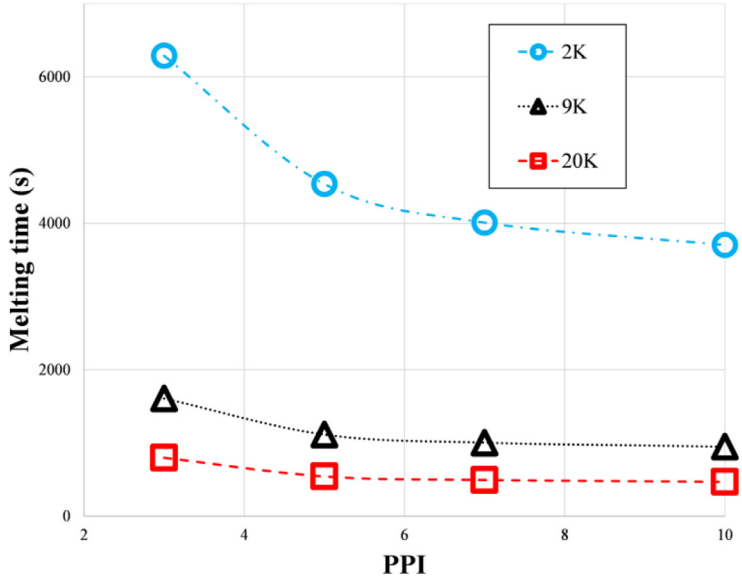

Fig. 12. Melting time versus PPI for different temperature difference (T_w - T_m) of 0.95 porosity copper periodic structure.

spectively, for the bottom heating scenario. Compared to the lateral heating curve, the curve of basal heating is less steep for the scope of PPI = 3 and 7, which implies the trend of curve may transform to parabolic fashion if the natural convection is strengthened. But for the present studied cases, purely altering the enclosure orientation cannot adjust the critical PPI.

4.3. Effect of thermal boundaries

Another parameter to be examined is the wall temperature. Note that the temperature difference (T_w - T_m) cannot only affect the convection strength, but it also influences the conduction heat transfer in the same way. Based on the 0.95 porosity copper periodic structure, two more wall temperatures (T_w - T_m = 2 K and 20 K) are numerically simulated.

The melting times of three different wall temperatures (T_w - T_m = 2 K, 9 K and 20 K) versus PPI are reported in Fig. 12. It is found that the slope of the 2 K curve is relatively sharper while the slope lessens as the wall temperature increases. Quantitively, the melting times of PPI = 3, 5, 7 and 10 are 6286 s, 4536. 2s, 4007.6 s and 3703.8 s, respectively, for a 2 K temperature difference while they are 796.2 s, 541. 4 s, 493 s and 467 s, respectively, for T_w - T_m = 20 K. The simulated results indicate that the optimal cell size cannot be altered through varying wall temperatures.

5. Conclusions

In this work, the critical cell size of a periodic structure, which is used as the thermal enhancer for PCM melting, is numerically studied. By definition, the critical cell size relates to thermal optimisation with melting rate enhancement while, for the present study, the critical cell size could generate the least melting time for a constant mass of PCM. Generic analysis was initially carried out to clarify possible relevant parameters, which consist of porosity and material properties of periodic structures in a given enclosure and the enclosure length. Effects of porosities (0.75, 0.8, 0.85, and 0.95) and materials (copper, aluminium, nickel, and stainless-steel) of periodic structures for a fixed-length (L = 25.4 mm) enclosure, enclosure length (L, 2L and 3L), enclosure orientation (top, lateral, and basal heating) and wall temperature (T_w-T_m = 2 K, 9 K and 20 K) were numerically investigated. It was found that

1) The incorporation of periodic structure can change the melting sequences of PCM, where a high thermal-diffusivity-ratio between ligament and PCM could lead to localised melting behaviour, where its occurrence may exist if $\phi=(d_p/L)\sqrt{\alpha_{ligament}/\alpha_{PCM}} > 1$.
2) For a fixed enclosure of PCM-periodic structure system, increasing porosity and/or reducing thermal conductivity (or thermal-diffusivity-ratio) of the periodic structure enlarges the critical cell size (or lower the critical PPI). In particular, the critical PPIs of copper- and aluminium-made periodic structures for all studied porosities are 10; for nickel, the critical values are 10 PPIs for 0.75, 0.8 and 0.85 porosities while it becomes 5 PPI for the 0.95 porosity. The critical PPIs of stainless-steel structures are 5 for the 0.75 porosity scenario and 3 for higher porosities.
3) Elongating the length of a PCM-periodic structure enclosure will lead to a lower critical PPI. For the investigated 0.95 porosity copper periodic structure, the critical cell sizes are 10 PPI for the L-enclosure, 5 PPI for the 2L-enclosure and 3 PPI (or less) for the 3L-enclosure, respectively
4) Varying the orientation or wall temperatures cannot modify effectively the critical cell size for the considered periodic structures.

In a nutshell, implications of periodic structure properties, enclosure parameters and thermal boundaries on critical cell size have been clearly clarified. The results can serve as a guideline for the design of relevant periodic structures while it can be also extended to other thermal enhancer configurations used in LHTES, thereby accelerating the commercial uptake of intermittent renewable energies.

Declaration of Competing interest

The authors declare that they have no known competing financial interests or personal relationships that could have appeared to influence the work reported in this paper.

Acknowledgements

This research was performed as part of the Australian Solar Thermal Research Institute (ASTRI), a project supported by the Australian Government, through the Australian Renewable Energy

Agency (ARENA). The first author, Chunrong Zhao, would also like to thank Queensland Geothermal Energy Centre of Excellence at The University of Queensland and China Scholarship Council (CSC) for the financial support.

References

[1] C.R. Zhao, M. Opolot, M. Liu, F. Bruno, S. Mancin, K. Hooman, Phase Change Behaviour Study of PCM Tanks Partially Filled with Graphite Foam, Applied Thermal Engineering (2021) 117313.
[2] Q.L. Ren, P.H. Guo, J.J. Zhu, Thermal management of electronic devices using pin-fin based cascade microencapsulated PCM/expanded graphite composite, International Journal of Heat and Mass Transfer 149 (2020) 119199.
[3] Y Mahmoudi, K Hooman, K Vafai, Convective heat transfer in porous media, CRC Press, 2019.
[4] W.J. Cao, C.R. Zhao, Y.W. Wang, F.M. Jiang, Thermal modeling of full-size-scale cylindrical battery pack cooled by channeled liquid flow, International journal of heat and mass transfer 138 (2019) 1178–1187.
[5] G.H. Bagheri, M.A. Mehrabian, K. Hooman, Numerical study of the transient behaviour of a thermal storage module containing phase-change material, Proceedings of the Institution of Mechanical Engineers, Part A: Journal of Power and Energy 224 (4) (2010) 505–516.
[6] M. Liu, S. Riahi, R. Jacob, F. Bruno, Design of sensible and latent heat thermal energy storage systems for concentrated solar power plants: Thermal performance analysis[J], Renewable Energy 151 (2020) 1286–1297.
[7] C.Y. Wang, M. Mobedi, A comprehensive pore scale and volume average study on solid/liquid phase change in a porous medium, International Journal of Heat and Mass Transfer 159 (2020) 120102.
[8] S. Mancin, A. Diani, L. Doretti, K. Hooman, Experimental analysis of phase change phenomenon of paraffin waxes embedded in copper foams, International Journal of Thermal Sciences 90 (2015) 79–89.
[9] Y.B. Tao, Y.L. He, A review of phase change material and performance enhancement method for latent heat storage system, Renewable and Sustainable Energy Reviews 93 (2018) 245–259.
[10] P.P. Levin, A. Shitzer, G. Hetsroni, Numerical optimization of a PCM-based heat sink with internal fins, International Journal of Heat and Mass Transfer 61 (2013) 638–645.
[11] R. Kalbasi, M. Afrand, J. Alsarraf, M.D. Tran, Studies on optimum fins number in PCM-based heat sinks, Energy 171 (2019) 1088–1099.
[12] N. Sharifi, T.L. Bergman, A. Faghri, Enhancement of PCM melting in enclosures with horizontally-finned internal surfaces, International Journal of Heat and Mass Transfer 54 (19-20) (2011) 4182–4192.
[13] X. Yang, Z. Lu, Q. Bai, Q. Zhang, L. Jin, J. Yan, Thermal performance of a shell-and-tube latent heat thermal energy storage unit: Role of annular fins, Applied Energy 202 (2017) 558–570.
[14] C.R. Zhao, M. Opolot, M. Liu, F. Bruno, S. Mancin, K. Hooman, Numerical study of melting performance enhancement for PCM in an annular enclosure with internal-external fins and metal foams, International Journal of Heat and Mass Transfer 150 (2020) 119348.
[15] K. Lafdi, O. Mesalhy, S. Shaikh, Experimental study on the influence of foam porosity and pore size on the melting of phase change materials, Journal of Applied Physics 102 (8) (2007) 083549.
[16] S.S. Sundarram, W. Li, The effect of pore size and porosity on thermal management performance of phase change material infiltrated microcellular metal foams, Applied Thermal Engineering 64 (1-2) (2014) 147–154.
[17] B.V.S. Dinesh, A. Bhattacharya, Comparison of energy absorption characteristics of PCM-metal foam systems with different pore size distributions, Journal of Energy Storage 28 (2020) 101190.
[18] M. Opolot, C.R. Zhao, M. Liu, S. Mancin, F. Bruno, K. Hooman, Influence of cascaded graphite foams on thermal performance of high temperature phase change material storage systems, Applied Thermal Engineering 180 (2020) 115618.
[19] A. Parida, A. Bhattacharya, P. Rath, Effect of convection on melting characteristics of phase change material-metal foam composite thermal energy storage system, Journal of Energy Storage 32 (2020) 101804.
[20] A. Pizzolato, A. Sharma, K. Maute, A. Sciacovelli, V. Verda, Design of effective fins for fast PCM melting and solidification in shell-and-tube latent heat thermal energy storage through topology optimization, Applied Energy 208 (2017) 210–227.
[21] G. Righetti, L. Doretti, C. Zilio, G.A. Longo, S. Mancin, Experimental investigation of phase change of medium/high temperature paraffin wax embedded in 3D periodic structure, International Journal of Thermofluids 5 (2020) 100035.
[22] M. Opolot, C.R. Zhao, M. Liu, S. Mancin, F. Bruno, K. Hooman, Investigation of the effect of thermal resistance on the performance of phase change materials, International Journal of Thermal Sciences 164 (2021) 106852.
[23] C.R. Zhao, M. Opolot, M. Liu, F. Bruno, S. Mancin, R. Flewell-Smith, K. Hooman, Simulations of melting performance enhancement for a PCM embedded in metal periodic structures, International Journal of Heat and Mass Transfer 168 (2021) 120853.
[24] M.A. Hayat, H.M. Ali, M.M. Janjua, W. Pao, C.H. Li, M. Alizadeh, Phase change material/heat pipe and Copper foam-based heat sinks for thermal management of electronic systems, Journal of Energy Storage 32 (2020) 101971.
[25] M. Al-Jethelah, S Ebadi, K. Venkateshwar, S.H. Tasnim, S. Mahmud, A. Dutta, Charging nanoparticle enhanced bio-based PCM in open cell metallic foams: An experimental investigation, Applied Thermal Engineering 148 (2019) 1029–1042.
[26] A. Pizzolato, A. Sharma, K. Maute, A Sciacovelli, V. Verda, Multi-scale topology optimization of multi-material structures with controllable geometric complexity—Applications to heat transfer problems, Computer Methods in Applied Mechanics and Engineering 357 (2019) 112552.
[27] C.R. Zhao, M. Opolot, M. Liu, J. Wang, F. Bruno, S. Mancin, K. Hooman, Review of Analytical Studies of Melting Rate Enhancement with Fin and/or Foam Inserts, Applied Thermal Engineering 207 (2022) 118154.
[28] C.R. Zhao, Y.B. Sun, J. Wang, K. Hooman, The Applicability of Volume-Averaging Method to Simulate Melting in a Multi-Scaled Periodic Structure, Energy 248 (2022) 123636.
[29] R. Akhilesh, A. Narasimhan, C. Balaji, Method to improve geometry for heat transfer enhancement in PCM composite heat sinks, International Journal of Heat and Mass Transfer 48 (13) (2005) 2759–2770.
[30] K. Hooman, N. Dukhan, A theoretical model with experimental verification to predict hydrodynamics of foams, Transport in porous media 100 (3) (2013) 393–406.
[31] P. Jany, A. Bejan, Scaling theory of melting with natural convection in an enclosure, International Journal of Heat and Mass Transfer 31 (6) (1988) 1221–1235.
[32] M. Opolot, C.R. Zhao, M. Liu, S. Mancin, F. Bruno, K. Hooman, A review of high temperature ($\geq 500^{\circ}$C) latent heat thermal energy storage, Renewable and Sustainable Energy Reviews 160 (2022) 112293.
[33] A.D. Brent, V.R. Voller, K.T.J. Reid, Enthalpy-porosity technique for modeling convection-diffusion phase change: application to the melting of a pure metal, Numerical Heat Transfer, Part A Applications 13 (3) (1988) 297–318.
[34] H. Shmueli, G. Ziskind, R. Letan, Melting in a vertical cylindrical tube: Numerical investigation and comparison with experiments, International Journal of Heat and Mass Transfer 53 (19-20) (2010) 4082–4091.
[35] M. Fadl, P.C. Eames, Numerical investigation of the influence of mushy zone parameter Amush on heat transfer characteristics in vertically and horizontally oriented thermal energy storage systems, Applied Thermal Engineering 151 (2019) 90–99.
[36] B. Kamkari, H. Shokouhmand, F. Bruno, Experimental investigation of the effect of inclination angle on convection-driven melting of phase change material in a rectangular enclosure, International Journal of Heat and Mass Transfer 72 (2014) 186–200.